Characterizing Graphene, Graphite, and Carbon Nanotubes by Raman Spectroscopy

M.S. Dresselhaus,[1] A. Jorio,[2] and R. Saito[3]

[1]Department of Physics and Department of Electrical Engineering and Computer Science, Massachusetts Institute of Technology, Cambridge, Massachusetts 02139; email: millie@mgm.mit.edu

[2]Departamento de Fisica, Universidade Federal de Minas Gerais, Belo Horizonte 30123-970, Brazil

[3]Department of Physics, Tohoku University, Sendai 980-8578, Japan

Abstract

Recent advances in Raman spectroscopy for characterizing graphene, graphite, and carbon nanotubes are reviewed comparatively. We first discuss the first-order and the double-resonance (DR) second-order Raman scattering mechanisms in graphene, which give rise to the most prominent Raman features. Then, we review phonon-softening phenomena in Raman spectra as a function of gate voltage, which is known as the Kohn anomaly. Finally, we review exciton-specific phenomena in the resonance Raman spectra of single-wall carbon nanotubes (SWNTs). Raman spectroscopy of SWNTs has been especially useful for understanding many fundamental properties of all sp^2 carbons, given SWNTs can be either semiconducting or metallic depending on their geometric structure, which is denoted by two integers (n,m).

1. GENERAL INTRODUCTION OF THE RESONANCE RAMAN EFFECT

Analysis of the observed Raman spectra and the resonance condition, when combined with theory, provides precise information on the electronic states, the phonon energy dispersion, and the electron-phonon interaction in sp^2 carbon systems. The resonance Raman effect in sp^2 carbons is briefly introduced in this section and is further developed subsequently.

1.1. The Resonance Raman Effect

Raman spectroscopy is an experimental technique that is commonly used to characterize all sp^2 carbons from three to zero dimensions (3D, 0D), such as 3D graphite, 2D graphene, 1D carbon nanotubes, and 0D fullerenes (1–5). Raman spectroscopy of sp^2 carbons provides not only unique vibrational and crystallographic information, but also unique information about physical properties that are relevant to electrons and phonons (6, 7). When a Raman process is combined with the optical absorption to (or emission from) an excited state, the Raman intensity is enhanced significantly (∼1000 times larger intensity) by a process called resonance Raman spectroscopy (12). Due to the resonance effect, we can observe the Raman signal even from a single layer of graphene (1-LG), that is, an atomic layer of the hexagonal lattice of carbon, or from an isolated single-wall carbon nanotube (SWNT). Analysis of the observed Raman spectra and the resonance condition, when combined with theory, provides precise information on the electronic states, phonon energy dispersion, and el-ph interaction in sp^2 carbon nanostructures.

1.2. Graphene: The Mother Structure of sp^2 Carbons

For 1-LG, which is the mother of all sp^2 carbons, there are two atoms, A and B, per unit cell, as shown in **Figure 1a**. By stacking graphene layers in an AB Bernal stacking arrangement, we get multilayer graphene (M-LG) or 3D graphite. Rolling up a 1-LG into a cylinder in a seamless way results in an SWNT whose geometrical structure is determined by two integers (n,m), which provide information about the nanotube diameter and chiral angle (5). Most sp^2 carbons do not have an energy gap at the Fermi level, and thus we always get a resonance condition for Raman spectra for any laser excitation energy. In the case of SWNTs, however, depending on (n,m), two (one) of three SWNT geometries show a semiconducting (metallic) behavior, and thus we must adjust the laser energy for obtaining a resonance condition, where an increase of several orders of magnitude in the intensity of the Raman signal occurs because of the strong localization of the peaks in the density of states of one-dimensional SWNTs (5). The resonant behavior for metallic SWNTs and graphene is different because SWNTs are one dimensional and graphene is two dimensional, and they have differences in their electronic density of states (5).

1.3. The G and G′ Bands

The Raman spectra of 1-LG consist of two dominant Raman-allowed spectral features (see **Figure 2a**). One is associated with the longitudinal optical (LO) phonon mode, occurring around 1580 cm^{-1} and is called the G band, and the other is an especially intense second-order dispersive Raman feature called the G′ band (or 2D band). The G′-band frequency depends on the laser excitation energy, E_{laser} (dispersive behavior) and appears
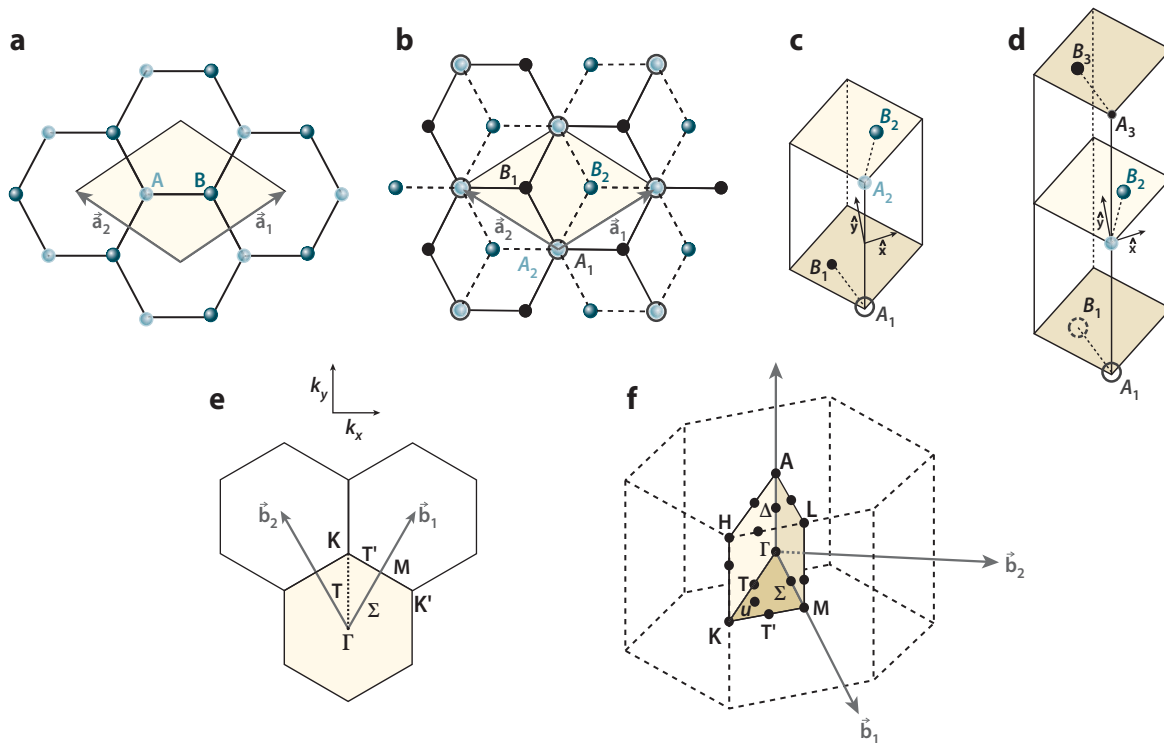
Figure 1

(*a*) A top view of the real-space unit cell of monolayer graphene (1-LG) showing the inequivalent atoms A and B and the unit vectors a$_1$ and a$_2$. (*b*) A top view of the real-space unit cell of bilayer graphene (2-LG). The light/dark blue dots and the black circles/black dots represent the carbon atoms in the upper and lower layers, respectively, of 2-LG. (*c*) The unit cell and the $\hat{x}$ and $\hat{y}$ unit vectors of 2-LG and (*d*) the same as part *c*, but for trilayer graphene (3-LG). (*e*) The reciprocal space unit cell showing the first Brillouin zone (BZ) with its high-symmetry points and lines, such as the T point connecting Γ to K Σ connecting Γ to M; and T$'$ connecting K to M. The two primitive vectors, k_x and k_y, on the top of the three hexagons show the reciprocal space coordinate axes. (*f*) The BZ for 3D graphite, showing the high-symmetry points and axes. Here Δ is a high-symmetry point along the axis connecting points A and Γ, and u is a general point in the KMΓ plane (6).

at ~2700 cm^{-1} for $E_{\text{laser}} = 2.414$ eV (1). For varying layer numbers in M-LG, the Raman spectra show different spectral widths and relative intensities of G to G$'$, reflecting the interlayer interaction between graphene layers (6). For example, the 1-LG Raman spectra can be distinguished from other spectra because the G$'$ band is stronger than the G band, whereas for 2-LG or M-LG, the G$'$ band is broader and weaker than the G band. Furthermore, a phonon-softening phenomenon for the G band appears by applying a gate voltage. This is known as the Kohn anomaly, which is important for determining the Fermi energy (E_F) position by Raman spectroscopy (8, 9, 67).

1.4. The Disorder-Induced D Band

Finite-size graphene has edges with special shapes, stacking disorder between two layers, and atomic defects within the layer. For such a disordered carbon, the D-band feature appears at ~1350 cm^{-1} for $E_{\text{laser}} = 2.414$ eV. The relative intensity of D to G provides
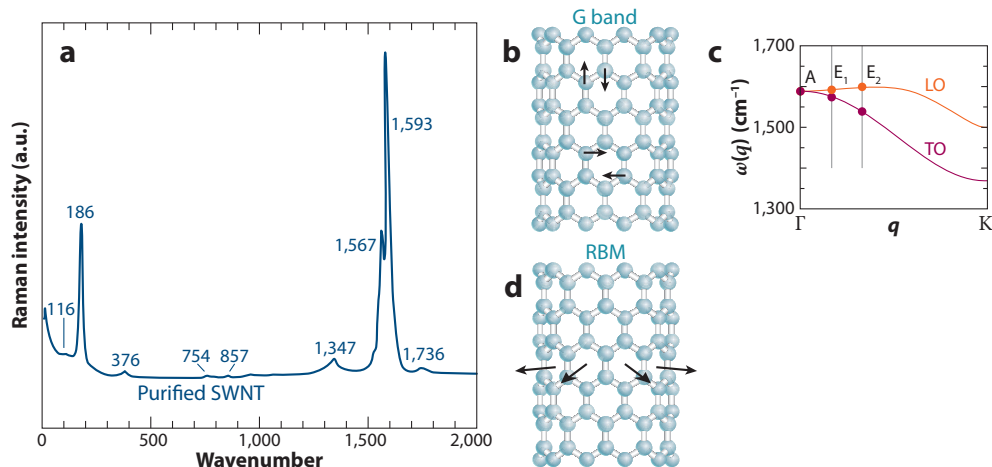
Figure 2

(*a*) Room-temperature Raman spectrum from a SWNT bundle grown by the laser vaporization method. (*b*) The G-band eigenvectors for the C-C bond stretching mode. The G band is composed of up to six peaks that are allowed in the first-order Raman spectra. The vibrations are tangential to the tube surface, three along the tube axis (LO) and three along the circumference (TO). (*c*) Within the set of three peaks, what changes is the relative phase of the vibrations, containing zero, two, or four nodes along the tube circumference, which is related to increasing the phonon wave vector, *q*, in the unfolded graphene phonon dispersion, $\omega(q)$. (*d*) Eigenvectors for the radial breathing mode (RBM) that appears around 186 cm^{-1} in part *a*.

a good indicator for determining the in-plane crystallite size or the amount of disorder in the sample (10, 11). Both the D and G′ bands are related to non-zone-center phonons, and the dispersive behavior is explained by a double-resonance Raman process (3). Confocal Raman spectra taken with a 1-μm diameter of the incident light provide a Raman intensity map over the sample, which yields edge structure information (4).

1.5. Radial Breathing Mode in SWNTs

The cylindrical geometry of an SWNT splits the G band into LO and tangential optical (TO) modes whose frequencies depend on the diameter, the Fermi energy (E_F), and the metallicity of the SWNT (2). Quantum confinement of the electron and phonon structures specifies discrete *k* values around the circumferential direction, which is useful for understanding the *k*-dependent el-ph interaction. Furthermore, the cylindrical shape of the SWNT introduces another Raman feature, the radial breathing mode (RBM), whereby each atom in the SWNT is vibrating in the radial direction. Because the RBM frequency is inversely proportional to the diameter, the (*n*,*m*) indices of an isolated SWNT can be assigned when considering the resonance condition (13). This article reviews what we learn about graphene, graphite, and carbon nanotubes, emphasizing the unique aspects of their complementary Raman spectra.

1.6. History of Graphite Raman Spectroscopy

Raman spectroscopy of graphitic materials has played an important role in their structural characterization since the 1970s (4, 10, 15), and this technique has also become a powerful tool for understanding the behavior of electrons and phonons in graphene (1, 16). Of the

three sp^2 carbon materials discussed in this review, graphite is by far the earliest material to have been investigated experimentally; however, in so doing, the earliest models for the electronic structure, dating back to the works of McClure (17) and Slonczewski & Weiss (18) in the 1950s, all considered 1-LG (5) as the fundamental building block for their increasingly sophisticated models. For this reason, there was much excitement in the sp^2 carbon research community when 1-LG was first prepared in the laboratory from highly oriented pyrolytic graphite in 2004 and studied experimentally (19, 20).

Therefore, interest in studying the fundamental properties of graphene grew rapidly with the discovery of an easy method to fabricate and identify these structures (19), especially after the unusual quantum Hall effect in these systems was reported (21). We now review the role that Raman spectroscopy has played in advancing research on graphene, graphite, and carbon nanotubes, highlighting some recent contributions to this topic. This review is not intended to be a comprehensive overview of the field but rather is intended to provide an overview of some of the major advances that have been made in the last decade, and to direct readers to the literature where more complete coverage can be found (1, 7).

2. GRAPHENE

Here, we show how to characterize graphene by Raman spectroscopy.

2.1. Structure of Graphene: AB Stacking

Graphene consists of sp^2 carbon hexagonal networks, in which strong covalent bonds are formed between two adjacent carbon atoms. The unit cell for M-LG contains two carbon atoms, A and B, each forming a triangular 2D network, but displaced from each other by the carbon-carbon distance $a_{C-C} = 0.142$ nm, as shown in **Figure 1a**.

The 3D graphite structure corresponds to a stacking of the hexagonal networks of individual graphene layers in the direction perpendicular to the layer plane (c axis) in an AB (or Bernal) stacking arrangement, in which the vacant centers of the hexagons on one layer have carbon atoms on hexagonal corner sites on the two adjacent graphene layers, as shown in **Figure 1b**. In graphite with AB stacking, the unit cell consists of four carbon atoms, (A_1, B_1) and (A_2, B_2), on the two-layer planes shown in **Figure 1b**, where the (A_1, B_1) bonds and (A_2, B_2) bonds are staggered across planes, as shown in **Figure 1b** and **Figure 1c**. The in-plane and c-axis lattice constants for graphite are $a = \sqrt{3}a_{C-C} = 0.246$ nm and $c = 0.670$ nm (interlayer distance $= 0.335$ nm), respectively. Normally, the bilayer graphene (2-LG) samples obtained by the mechanical exfoliation of graphite exhibit (22) an AB stacking arrangement, and therefore the number of atoms in the unit cell of 2L graphene is the same as that for graphite, with four atoms per unit cell, as shown in **Figure 1c**. Trilayer graphene (3-LG), in turn, contains three layers, two of which are like 2-LG, and the third layer has carbon atom A_3 over A_1 and carbon atom B_3 over B_1, as shown in **Figure 1d**. Four-layer graphene (4-LG) consists of the stacking of two unit cells of the type shown in **Figure 1c**, one stacked on top of the other. Thus, **Figure 1** summarizes the in-plane structure of graphene, and the interlayer stacking order of graphite and few-layer graphene. Actual graphene samples prepared by chemical vapor deposition (CVD) or from an SiC precursor by other synthesis methods may have different stacking ordering (see Section 2.2) and therefore different properties and Raman spectra. The corresponding reciprocal space structure is discussed in Section 2.3. Given that carbon nanotubes have

curvature and chirality, their structure includes a description of their diameter and chiral angles usually expressed in terms of the two integers (n,m), as summarized in Section 1.2 and in much more detail elsewhere (1, 7).

2.2. Sample Preparation of Graphene

In the early days of graphene studies, graphene samples were mainly prepared by the mechanical exfoliation of HOPG (highly oriented pyrolytic graphite) (22), although earlier preparation of 1-LG had been demonstrated as early as 2001 based on a nano-diamond precursor material (23). Both approaches led to M-LG samples with AB Bernal stacking. An SiC-based precursor method provides an alternate route for preparing graphene samples (24, 25) and leads to a graphene family of materials with significant interaction with the SiC substrate, which results in somewhat different properties than graphene samples produced by the mechanical exfoliation from HOPG, particularly with respect to stacking order. For example, the mechanical exfoliation of HOPG leads to highly ordered Bernal AB stacking, whereas few-layer graphenes synthesized from SiC show partial AB Bernal layer stacking order.

Epitaxial CVD growth of graphene using various transition metal catalysts, such as Ni and Cu, has also been demonstrated (26), and this approach to graphene synthesis is still under active development. Experiments described in this review are carried out on graphene samples sitting on various substrates (such as Si–SiO$_2$), freely suspended, chemically doped, or gated to control the Fermi level. Freely suspended graphene tends to have a higher mobility (with values as high as 200,000 cm^2/Vs at the room temperature) than its graphene counterparts on substrates.

2.3. The Reciprocal Space of Graphene

In reciprocal space, the graphene Brillouin zone (BZ) is as shown in **Figure 1e** for 1-LG, and the atomic motion in the z direction normal to the plane requires a third direction. **Figure 1e** also shows some high-symmetry points within the first BZ of 1-LG: the Γ point at the zone center, the M point in the middle of the hexagonal sides, and the K and K' points at the corners of the 2D hexagonal BZ. Points K and K' are inequivalent because they are not connected by reciprocal lattice vectors. In contrast, the reciprocal space for bilayer graphene contains a symmetry plane for $k_z = 0$ (the K point) and another for $k_z = \pi/c$ (the H point), forming the lower and upper planes of the BZ for 2-LG, as shown in **Figure 1f**. This unit cell also represents the BZ for 3D graphite and for all graphenes with an even number of layers.

2.4. Phonon Dispersion of sp^2 Carbons

An understanding of the phonon dispersion of sp^2 carbons is essential to interpret their Raman spectra. Because the unit cell of 1-LG contains two carbon atoms, A and B, there are six phonon dispersion branches for sp^2 carbons (see **Figure 3**), in which three are acoustic (A) branches and the other three are optic (O) phonon branches. For one acoustic branch (A) and one optic (O) phonon branch, the atomic vibrations are perpendicular to the graphene plane, and they correspond to the out-of-plane (o) phonon modes. For two acoustic and two optic phonon branches, the vibrations are in-plane (i). Furthermore, the phonon modes are classified as longitudinal (L) or transverse (T) according to whether
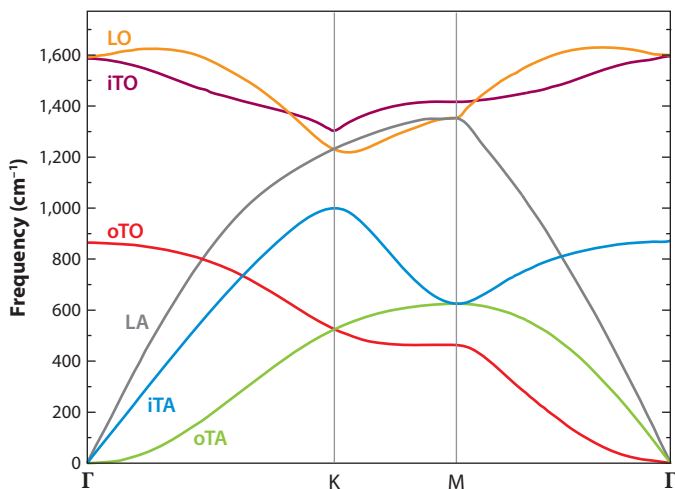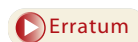
Figure 3

Calculated phonon dispersion relation of graphene showing the LO, iTO, oTO, LA, iTA, and oTA phonon branches (adapted from Reference 14).

Erratum

the vibrations are parallel or perpendicular to the wave-propagating direction specified by the wave vector k. The longitudinal acoustic (LA) and the longitudinal optical (LO) modes are always in-plane modes along with the iTA and iTO modes, which are normal to the LA and LO modes. In addition, there are two out-of-plane modes denoted by oTA and oTO that are normal to the other four modes. Therefore, along the high-symmetry $\Gamma - K$ or $\Gamma - M$ directions, the six phonon dispersion curves are assigned to LO, iTO, oTO, LA, iTA, and oTA phonon modes (see **Figure 3**). These phonon dispersion relations are used to characterize graphene, graphite, and carbon nanotubes.

At the zone center (Γ point), the in-plane iTO and LO optic modes correspond to the vibrations of the sublattice A against the sublattice B, and these modes are degenerate at the Γ point. According to group theory, the degenerate zone-center LO and iTO phonon modes belong to the two-dimensional E_{2g} representation, and therefore, they are Raman-active modes (5, 27, 28). The degeneracy of the LO and iTO phonons is lifted for general points inside the BZ for SWNTs or by applying an external stress to graphene or to SWNTs (29).

The phonon modes around the K point are especially important because the D band and G′ band are related to phonon modes in the vicinity of the K point. Exactly at the K point, the phonon that comes from the iTO branch is nondegenerate. The LO and LA phonon branches meet each other at the K point in the BZ, resulting in a doubly degenerate phonon mode (30).

2.5. The Double-Resonance Raman Process

In a first-order Raman process, light is absorbed with the energy and momentum of the incident photon, and the scattered light is typically downshifted by the energy of a phonon with momentum equal to the momentum difference between the incident and scattered light. The wave vector of the phonons thus produced are therefore very small compared to

the size of the BZ. These phonons near the Γ point are Raman-active modes in the solid state. In a second-order Raman process, the requirement of $q \sim 0$ is relaxed, and a pair of $q \neq 0$ phonons with wave vectors q and $-q$ are relevant. The second- (and higher-) order Raman processes generally give a broad background signal in the Raman spectra. Such higher-order processes can have large intensities, comparable to the first-order process when two of the three intermediate states in the two-phonon scattering (or one-phonon and one-elastic scattering) process are real electronic states. Then, the double-resonance (DR) effect results in spectral features as intense as the first-order resonance Raman process. We call such processes DR Raman processes (3, 31, 32) and because of the DR effect, sp^2 carbons show a strong first-order G-band feature as well as strong second-order DR G′-band and D-band features.

In the DR process, two scattering events for $q \neq 0$ occur. One scattering event occurs near K (or K') and is called intravalley scattering. Another scattering event takes an electron from K to K' (or K' to K), which we call an intervalley scattering process. The D band (which involves one phonon and one elastic scattering events) and the G′ band (which involves two phonons) are both intervalley scattering processes, and thus the corresponding phonons are K point iTO phonon modes. The D* band (1620 cm^{-1}) is an intravalley process and involves a near Γ point phonon and an elastic scattering event. Both the D band and the D* band are symmetry-breaking processes, requiring an elastic scattering process to conserve momentum.

When E_{laser} is increased relative to the K point of graphene, where the valence and conduction bonds have the same energy, the resonance k vector for the electron increases in magnitude as k moves away from the K point. In the DR process, the corresponding q vector for the phonon, as measured from the K point, increases with increasing k for the electron. Thus, by changing the laser energy, we can observe the phonon energy along the phonon dispersion relations (**Figure 3**). This effect is observed experimentally as a change in the phonon frequency as a function of E_{laser} (32). A tunable laser system can directly show this dispersive behavior for the D band and the G′ band in their Raman spectra taken at different laser excitation energies.

In the case of 2-LG, there are four energy dispersions (two π for the valence band and two π' for the conduction band) near the K point. Thus, we have two states for the photo-excited state and for the first-phonon emitted state, and thus four possible DR processes exist. As such, we expect 4 G′ Raman spectra that have different $\omega(q)$ dispersion curves. This is why the 2-LG Raman intensity of the G′ band is smaller relative to that of the G band, and the G′-band feature for 2-LG is broader than that for 1-LG. According to calculations (33), the Raman intensity depends on each of the four DR processes. Similarly, for n-LG, we have n^2 possible DR processes, and the detailed Raman spectra and the intensities of their Raman-active DR features have been calculated (33), which will be useful for characterizing the Raman spectra observed for few-layer graphene.

2.6. The Kohn Anomaly in 1-LG

One goal for graphene science and technology is to fabricate high-frequency graphene devices. Although the mobility of carriers in graphene is attractively large, there are many challenges for making a device that exhibits (*a*) an energy gap, (*b*) a sufficiently large on-off ratio of the current in a switching device, and (*c*) fast control of the Fermi energy (E_F) position (6). When we apply a gate electrode and change the gate voltage, we can

obtain the response of the device as a function of the gate voltage (V_g). Although V_g is related to the Fermi energy (E_F), V_g is not proportional to E_F. Furthermore, the thickness of the insulator between the gate and the source electrode determines the sensitivity of the V_g to E_F. Thus, the determination of the value of E_F is an important subject.

It is important that Raman spectroscopy can be used to determine E_F by observing a phonon-softening phenomenon for the G-band phonon (see, for example, References 9 and 67). Because there is no energy gap in graphene, the G-band phonon for $\mathbf{q} = 0$ can excite an electron-hole pair near the Dirac point for energies $|E| < \hbar\omega/2 \sim 0.1\,\mathrm{eV}$ through the el-ph interaction. Then, the electron-hole pair recombines to emit a phonon, which causes a perturbation to the phonon: $\hbar\omega_\lambda = \hbar\omega_\lambda^{(0)} + \hbar\omega_\lambda^{(2)}$, where $\omega_\lambda^{(0)}$ is the original phonon frequency without the el-ph interaction and the perturbation term $\hbar\omega_\lambda^{(2)}$ is given by second-order perturbation theory,

$$\hbar\omega_\lambda^{(2)} = 2 \sum_{\mathbf{k}} \frac{|\langle \mathrm{eh}(\mathbf{k})| H_{\mathrm{int}} |\omega_\lambda\rangle|^2}{\hbar\omega_\lambda^{(0)} - (E_e(\mathbf{k}) - E_h(\mathbf{k})) + i\Gamma_\lambda} \qquad 1.$$
$$\times \big(f(E_h(\mathbf{k}) - E_F) - f(E_e(\mathbf{k}) - E_F)\big).$$

Here, the real part of $\omega_\lambda^{(2)}$ gives the phonon frequency shift from $\omega_\lambda^{(0)}$, whereas the imaginary part of $\omega_\lambda^{(2)}$ gives a spectral width of the Raman feature due to the fact that the phonon has a finite lifetime. In **Figure 4a**, we show a diagram for phonons with an energy dispersion for graphene. When the Fermi energy is shifted from the Dirac point, some excitation processes are suppressed by the Fermi distribution function $f(E(k))$. In **Figure 4b**, we show only the denominator of Equation 1 as a function of the excitation energy E, in the energy region $E < 0.2\,\mathrm{eV}$ ($E > 0.2\,\mathrm{eV}$), where the el-ph interaction contributes to the upshift (downshift) of the phonon frequency. Thus, when $2E_F \cong \pm 0.2\,\mathrm{eV}$, the phonon softening become a maximum, from which we can determine the Fermi energy position.
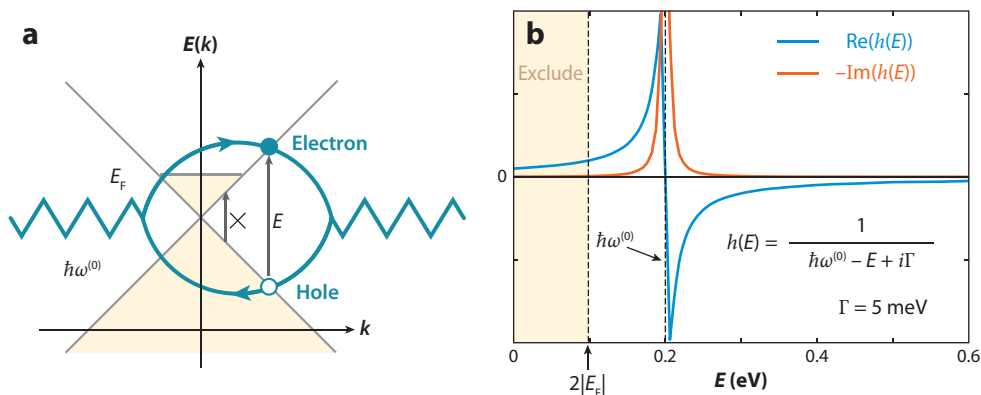

Figure 4

(*a*) An intermediate electron-hole pair state that contributes to the energy shift of the optical phonon modes is depicted. A phonon mode is denoted by a zig-zag line, and an electron-hole pair is represented by a loop. The low-energy electron-hole pair satisfying $0 \leq E \leq 2|E_F|$ is forbidden at zero temperature by the Pauli principle. (*b*) The energy correction to the phonon energy by an intermediate electron-hole pair state, where the sign of the correction depends on the energy of the intermediate state given by $h(E) = 1/(\hbar\omega^{(0)} - E + i\Gamma)$. The plot for the real and imaginary parts of $h(E)$ is made for $\Gamma = 5\,\mathrm{meV}$ (9, 67).

2.7. Kohn Anomaly in 2-LG

In **Figure 5a**, G-band spectra are shown for four different gate voltages. Two peaks are observed in the spectra whose frequencies behave oppositely for $+V_g$- and $-V_g$-applied gate voltages. The two G modes can be assigned to symmetric (S) and antisymmetric (AS) G bands whose atomic motions are shown in **Figure 5b**. If the two graphene layers in 2-LG are equivalent, group theory tells us that AS-G is not a Raman-active mode. However, because 2-LG is normally sitting on a substrate and V_g is inequivalently applied for the two layers, the two graphene layers are not equivalent, which allows observation by a symmetry-breaking substrate making the AS-G mode Raman active (16, 34). In **Figure 5c**, possible e-h pair excitations by S-G and AS-G phonons are shown, and these processes explain the different Kohn-anomaly behaviors observed in the Raman spectra (for details, see References 16 and 35).

3. RAMAN SPECTROSCOPY OF CARBON NANOTUBES

Next, we discuss the Kohn-anomaly effect in SWNTs where exciton formation is essential for understanding the observed spectra.

3.1. Kohn Anomalies of the G band of SWNTs

The Kohn-anomaly effect of the G band is observed for metallic SWNTs by using an electrochemical doping technique (8). In the case of SWNTs, the LO and iTO A symmetry phonon modes split into two peaks, denoted by G^+ and G^-, whose splitting in frequency ($\omega_{G^+} - \omega_{G^-}$) shows a different dependence on the SWNT diameter between metallic and semiconducting nanotubes (36). In the case of metallic SWNTs, the G^- peaks soften, broadening with an asymmetric spectral lineshape (37). To obtain the Raman spectra as a function of V_g, a solution of isolated SWNTs in an electrolyte is prepared, and the applied gate electrode is varied to provide electrochemical doping and variation of the Fermi level while E_{laser} is adjusted to the resonant exciton energy of the (*n*,*m*)-specified SWNT.
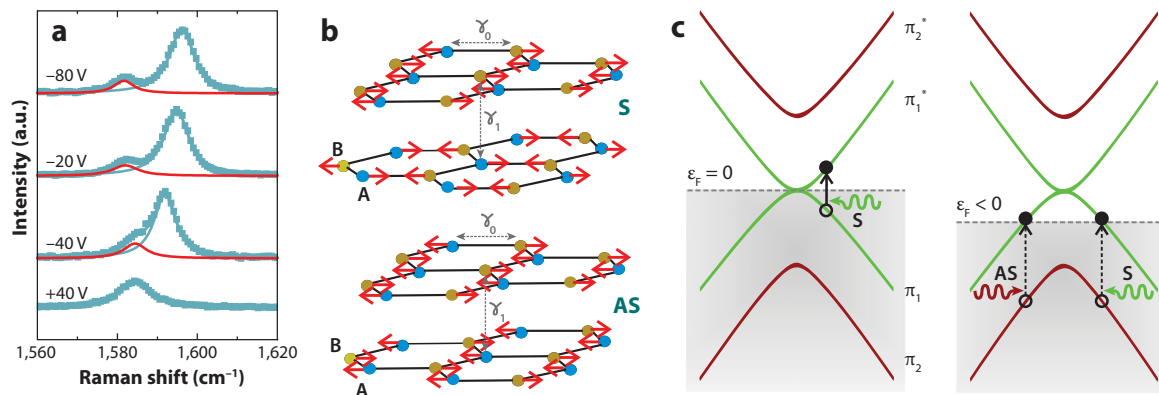

Figure 5

(*a*) Raman G-band spectra of 2-LG as a function of the gate voltage. Here S and AS denote symmetric and antisymmetric G-band modes, respectively, whose atomic motions are shown in part *b* by the arrows in the two layers for the S and AS modes. (*c*) Possible virtual excitations by the electron-phonon interaction, when a gate voltage, *E*, is applied and the S and AS G-band features are observed in the Raman spectra (34).

By changing the gate voltage, V_g, the LO and iTO phonons' (G-band) frequencies and their spectral widths are observed, thereby probing the dependence of the Raman spectra on the Fermi level. This characterization is also important for determining E_F for sp^2 carbon devices on a substrate. Electrochemical doping experiments thus use the variation of the Raman G-band spectrum to help assign the chirality of the nanotube, as is done in **Figure 6**. This figure shows two strong-intensity G-band peaks with different phonon frequencies. The higher-frequency peak does not depend on the gate voltage, and the lower-frequency peak shows a frequency shift with a strong broadening near the Dirac point. The existence of a flat-intensity peak as a function of the Fermi energy for a metallic SWNT indicates that the el-ph coupling is weak for the iTO phonon mode. Moreover, the nanotube shown in **Figure 6** is expected to have a chiral angle close to that of an armchair SWNT ($\theta = 30°$), given the el-ph coupling is shown to be strongly k dependent around the K point. Theory tells us that the chirality-dependent Kohn-anomaly response is strong for θ close to 30°, allowing observation of the Kohn-anomaly response (9, 67).

In **Figure 6a** and **Figure 6b**, we show experimental results of the G-band intensity as a function of applied gate voltage for two different isolated SWNTs. For the given laser excitation energy of 1.91 eV, the RBM frequencies of 196 and 193 cm^{-1} are observed for the samples of **Figure 6a** and **Figure 6b**, respectively. We can assign (n,m) values to each of these SWNTs by using the conventional assignment techniques for SWNTs based on measurement of their RBM frequencies under resonance conditions (13). Using this approach, the (n,m) values were assigned as (12,6) for **Figure 6a** and (15,3), (16,1), or (11,9) for **Figure 6b** (8).
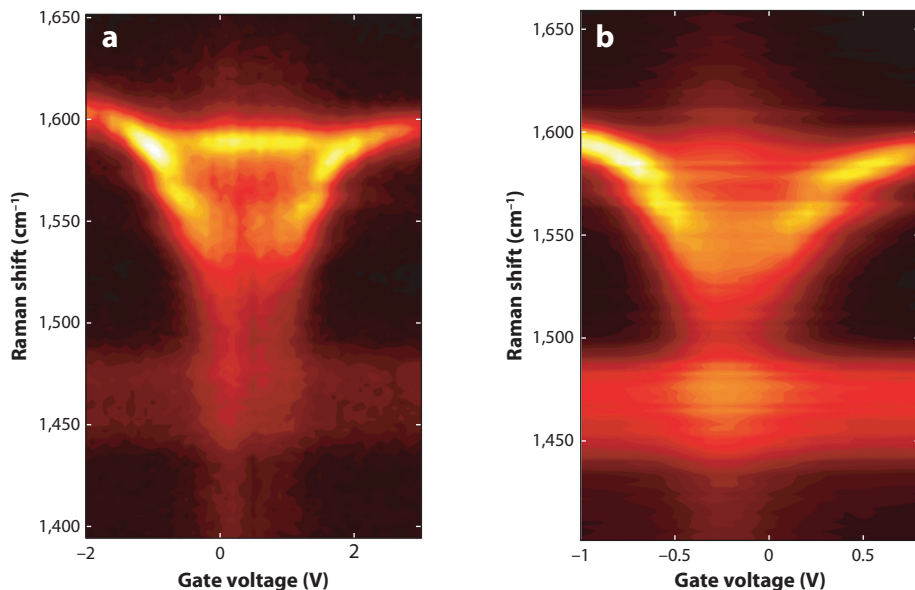

Figure 6

Experimental results of the Raman G-band intensity as a function of applied gate voltage for two metallic SWNTs: (*a*) a (12,6) M-SWNT and (*b*) a (15,3) or (16,1) M-SWNT. A strong (weak) intensity peak is denoted by the yellow (black) color (9).

Furthermore, from the following theoretical analysis, we can assign this SWNT either to (15,3) or to (16,1) for the SWNT for **Figure 6b**, and we can exclude (11,8).

3.2. The k-Dependent Electron-Phonon Interaction and the Kohn-Anomaly Effect

In **Figure 7**, we show the calculated G-band energy, $\hbar\omega_\lambda$ as a function of E_F for (*a*) a (15,0) zigzag nanotube, (*b*) a (10,4) chiral nanotube, and (*c*) a (10,10) armchair nanotube where $\hbar\omega_\lambda$ was studied by gate doping. The error bars in **Figure 7** denote the spectral width. The LO mode shows an energy shift and a broadening effect, whereas the iTO mode shows (**Figure 7a**) a hardening (an upshift in ω_{iTO}) and broadening, (**Figure 7b**) a lowering (a downshift in ω_{iTO}) and broadening, or (**Figure 7c**) no frequency response. The main reasons for the chirality-dependent Kohn-anomaly effect in SWNTs are that (*a*) the el-ph interaction is k dependent and (*b*) the cylindrical curvature shifts the 1D BZ (cutting line) away from the K point (for a detailed description, see References 9 and 67).

The experimental results for the relative intensity of the LO and iTO peaks as a function of (n,m) suggest the need to calculate the resonance frequencies and the corresponding resonance Raman intensities (38). For such calculations, it is important to know whether the resonance condition is satisfied. Using a tunable laser system, the RBM Raman excitation profile is investigated as a function of V_g (39), which shows a significant difference in the RBM intensity attenuation as a function of V_g between metallic and semiconducting SWNTs. A detailed comparison between measurement and theory also indicates that the RBM frequency shows a weak ($\sim$1 cm^{-1}) phonon softening, which depends on the SWNT diameter and chiral angle (40).

3.3. The RBM Measurement and the Experimental Kataura Plot

The optical transition energy, E_{ii}, as a function of the tube diameter that is obtained by the Raman excitation profile for each (n,m) SWNT, is called the Kataura plot (41, 42), and an example of such a plot is shown in **Figure 8**. The Kataura plot is frequently used for assigning (n,m) values from resonance Raman spectra (13) and photoluminescence spectra (43). Thus, many groups have made an effort to obtain E_{ii} values for a large range of SWNT diameters and over i values of E_{ii} up to six (see Reference 44).
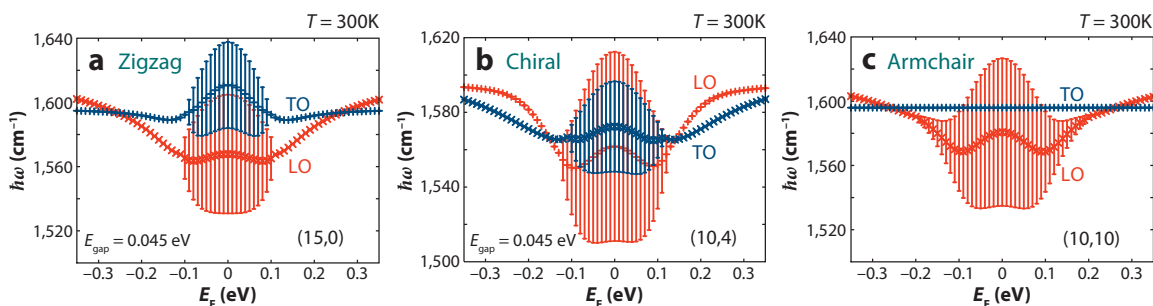

Figure 7

The E_F dependence of the LO and iTO phonon energies in the case of the (*a*) (15,0) zigzag nanotube, (*b*) a (10,4) chiral nanotube, and (*c*) a (10,10) armchair nanotube. The spectral width for each nanotube is plotted as an error bar (9, 67).

Figure 8a shows a 2D RBM Raman intensity map for the water-assisted CVD-grown (super-growth) SWNT sample (45, 46) as a function of the RBM frequencies $\omega_{\mathrm{RBM}}^{S.G.}$. Because $\omega_{\mathrm{RBM}}^{S.G.}$ is inversely proportional to the SWNT nanotube diameters, a plot called the experimental Kataura plot is used. This S.G. sample has a very broad diameter distribution, and the density of the sample is small (the individual SWNTs in the S.G. sample are well isolated from one another), and such properties are exploited in the construction of **Figure 8a**, in which 125 different laser lines were used (44). By fitting each of the spectra with Lorentzians, (n,m) indices were assigned to 197 different SWNTs, which is important for understanding the chirality dependence of the el-ph interaction, as shown below.

Figure 8b is a Kataura plot of all $E_{ii}^{S.G.}$ versus ω_{RBM} obtained experimentally by fitting the resonance windows extracted from the data in **Figure 8a**. The observed $E_{ii}^{S.G.}$ range from E_{11}^{S} to E_{66}^{S} (the superscript S here stands for S-SWNTs and M for M-SWNTs). Finally, all the $E_{ii}^{S.G.}$ data in **Figure 8b** can be fitted using an empirical equation that is discussed below and given by (47, 48)

$$E_{ii}(p, d_t) = \alpha_p \frac{p}{d_t} \left[1 + 0.467 \log \frac{0.812}{p/d_t} \right] + \beta_p \cos 3\theta / d_t^2, \qquad 2.$$

where p/d_t corresponds to the distance of the k point from the K point in the two-dimensional BZ of graphene (41, 49, 50), and p is defined as $1, 2, 3, \ldots, 8$ for E_{11}^{S}, E_{22}^{S},
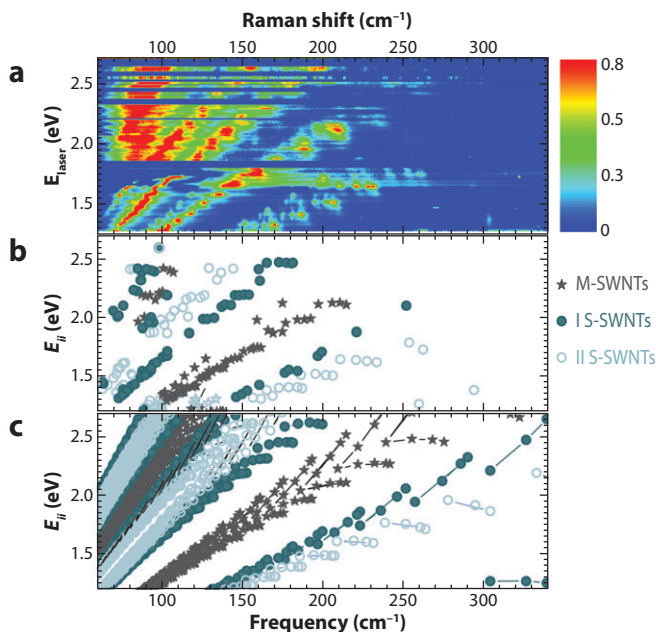

Figure 8

(*a*) An RBM resonance Raman map for the super-growth (*S.G.*) SWNT sample. (*b*) A Kataura plot of all transition energies ($E_{ii}^{S.G.}$) that could be obtained experimentally from the resonance windows extracted from part *a*, as a function of ω_{RBM}. (*c*) The Kataura plot obtained from Equation 2 with the parameters that best fit the data in part *b*. The gray stars stand for M-SWNTs [$(2n + m)\mathrm{mod}\,3 = 0$], the blue-green circles stand for type I S-SWNTs [$(2n + m)\mathrm{mod}\,3 = 1$], and the light blue circles stand for type II S-SWNTs [$(2n + m)\mathrm{mod}\,3 = 2$] (44).

$E_{11}^M, \ldots, E_{66}^S$. The parameter $\alpha_p = 1.074$ for $p = 1, 2, 3$, and $\alpha_p = 1.133$ for $p \geq 4$. The β_p values for the lower (upper) E_{ii} branches are –0.07(0.09), –0.18(0.14), –0.18(0.29), –0.33(0.49), –0.43(0.59), –0.60(0.57), –0.6(0.73), and –0.65(not measured) for $p = 1, 2, 3, \ldots, 8$, respectively (48, 51). The functional form in Equation 2 carries a linear dependence of E_{ii} on p/d_t, which is expected from the quantum confinement of the 2D electronic structure of graphene (5, 50), a logarithmic correction term that comes from many-body corrections (52) and a θ-dependent term that includes electronic trigonal warping and chirality-dependent curvature effects ($\sigma - \pi$ hybridization) (47, 53). The theoretical understanding of all these factors comes from theoretical calculations including the many-neighbors approximation in the tight-binding model, curvature effects through the $\sigma - \pi$ hybridization (54), and excitonic effects through solving the Bethe-Salpeter equation (55, 56). However, even by adding all these correction terms, the effect of dielectric screening must also be considered to achieve the required experimental accuracy, as described below.

3.4. Dielectric Screening of the Exciton Energy by the Surrounding Materials

Regarding the detailed understanding of the exciton energy of SWNTs, there is still a strong ongoing debate about the strength of the exciton-binding energy that is sensitive to the dielectric screening by the surrounding materials of the SWNTs, which is known as an environmental effect (53, 58–60). In **Figure 9**, the experimental E_{ii} values (solid dots) from **Figure 8b** and the calculated bright exciton energies, E_{ii}^{cal}, (open circles and stars) obtained with the dielectric screening constant, $\kappa = 1$, are compared (53). Here, κ is adopted as a
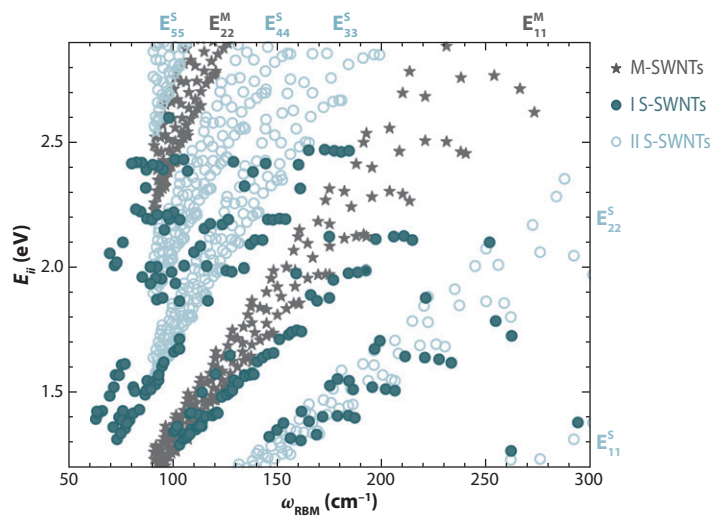

Figure 9

Solid dots show the E_{ii}^{exp} versus ω_{RBM} results in the Kataura plot obtained from resonance Raman spectra taken from a super-growth SWNT sample (44, 57). The light blue open circles (S-SWNTs) and the dark gray stars (M-SWNTs) give E_{ii}^{cal} calculated for the bright exciton with dielectric constant $\kappa = 1$ (56). Along the x axis, E_{ii}^{cal} values are translated using the relation $\omega_{RBM} = 227/d_t$ (57). Due to limited computer access, only E_{ii} for tubes with $d_t < 2.5$ nm (i.e., $\omega_{RBM} > 91$ cm^{-1}) have been calculated. Transition energies E_{ii}^S ($i = 1$ to 5) and E_{ii}^M ($i = 1, 2$) are plotted versus ω_{RBM}.

parameter in the calculation for describing the screening of the surrounding materials and of all electrons except for π electrons (55, 56, 61), which are considered explicitly. In a previous calculation, $\kappa = 2.22$ reproduced the experimental results well for a bundle SWNT sample, and only for E_{22}^S transitions and for a small range of diameters (56). However, a single value of κ was found to be insufficient for reproducing such a large diameter and energy region as is pertinent to the super-growth sample.

To model the dielectric constant, κ, we consider κ to consist of the screening of the e-h (electron-hole) pair by core (1s) electrons and by σ electrons (κ_{tube}) as well as by the surrounding materials (κ_{env}), and κ_{env} should be diameter dependent (59). For the screening by π electrons, we consider the polarization function, $\varepsilon(q)$, within the random-phase approximation (RPA) (56, 59, 62), in which the corresponding q should also depend on SWNT diameter. To fully account for the observed E_{ii}, the total κ values ($1/\kappa = C_{env}/\kappa_{env} + C_{tube}/\kappa_{tube}$) are fitted to minimize $E_{ii}^{exp} - E_{ii}^{cal}$. The obtained κ values can then be fit with the relation (57)

$$\kappa = C_\kappa^p \left(\frac{p}{d_t}\right)^{1.7}.$$ 3.

The integer, p, is defined in Equation 2, and C_κ is a coefficient that depends on p (53, 60). In fact, for E_{11}^S, E_{22}^S, and E_{11}^M, the value for C_κ is $C_\kappa = 0.75$ for the super-growth SWNTs and $C_\kappa = 1.02$ for the alcohol-assisted SWNTs. The E_{33}^S and E_{44}^S transition energies are fitted using $C_\kappa = 0.49$ for the super-growth and the alcohol-assisted samples.

Qualitatively, the origin of the diameter dependence of κ as given by Equation 3 consists of (a) the exciton size and (b) the amount of electric field probing the dielectric constant of the surrounding material. These two factors are connected, and the development of an electromagnetism model is needed to fully rationalize how they determine κ in Equation 3 (66).

3.5. RBM Frequency and Shifts Due to the Surrounding Material

The advances in understanding the optical transition energies for nanotubes were only made possible by the accurate (n,m) assignment procedures, which are closely related to the RBM frequency dependence on the SWNT diameter. In **Figure 10**, we compare similar ω_{RBM} Raman spectra taken from two different samples. The ω_{RBM} spectra for the super-growth SWNTs (orange lines) are compared to the ω_{RBM} spectra obtained from an SWNT sample grown by the alcohol-assisted CVD method (blue lines) (57). Comparing the spectra in **Figure 10a** and **Figure 10b**, it is clear that the ω_{RBM} values for the alcohol-assisted CVD sample are upshifted relative to those of the super-growth ω_{RBM} frequencies. For the super-growth sample, the $\omega_{RBM} = 227.0/d_t$ relation was found. All the ω_{RBM} results in the literature are upshifted from the values observed for the super-growth sample, and this difference has been explained as being due to the van der Waals interaction with the environment (arising from a substrate or from interaction with other SWNTs), which can be generally described by (57)

$$\omega_{RBM}^{Lit.} = \frac{227}{d_t}\sqrt{1 + C_e{}^* d_t^2},$$ 4.

where C_e is a fitting parameter that gives the effect of the environment on ω_{RBM}. C_e is theoretically described by $C_e = [6(1 - v^2)/Eh][K/s_0^2]$ (nm^{-2}), where v is the Poisson's ratio,
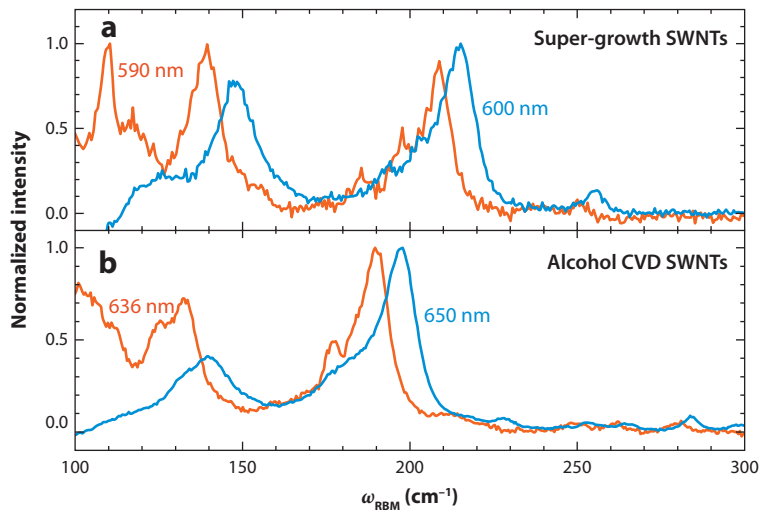
Figure 10

The ω_{RBM} spectra for (*a*) super-growth SWNTs (*orange*) and for (*b*) alcohol CVD SWNTs (*blue*). The spectra are obtained using different laser lines: (*a*) 590 nm (*orange*) and 600 nm (*blue*); (*b*) 636 nm (*orange*) and 650 nm (*blue*) (57).

Table 1   Strength of the environmental effect on the RBM frequency as measured by the C_e factor in Equation 4, which fits different SWNT samples in the literature

C_e	Sample	Reference
0	Water-assisted CVD	Araujo et al. (57)
0.05	HiPCO@SDS	Bachilo et al. (43)
0.059	Alcohol-assisted CVD	Araujo et al. (47)
0.065	SWNT@SiO$_2$	Jorio et al. (13)
0.067	Freestanding	Paillet et al. (63)

E is the Young's modulus, h represents the thickness of a shell pressing the SWNT through a van der Waals force, K gives the van der Waals interaction strength, and s_0 is the equilibrium separation between the SWNT wall and the environmental shell. **Table 1** gives the C_e values fitting the RBM results for several samples in the literature. For $d_t < 1.2$ nm, where the curvature effects become important, the environmental effect depends more critically on the specific sample (meaning C_e may change), and the observed environmental-induced upshifts range from 1 to 10 cm^{-1} for small-diameter tubes within bundles, or when wrapped by different surfactants (e.g., SDS or DNA).

3.6. Near-Field Raman Spectroscopy

Near-field Raman spectroscopy can observe spatially resolved Raman images for regions smaller than the wavelength of the light used. Here, we show recent results on the G′ band of SWNTs.

As with other sp^2 carbon spectra, the G′ band in the Raman nanotube spectra provides unique information about the electronic structure of S-SWNTs and M-SWNTs. Analogous to graphene, SWNTs show a dispersive behavior for the G′ band, but because of a sharp resonance at E_{ii}, the G′-band spectra are generally observed as a set of dots that represent many (n,m) tubes, each with its own E_{ii} value (64). However, for a nonhomogeneous surface or substrate, a continuous frequency dispersion is observed for the G′ band in SWNT bundles, where tubes experience a different environment when they enter or leave the E_{ii} resonance window (1, 2).

Besides the dimensionality effects, the presence of perturbations (e.g., doping) is expected to change the local electron and phonon structure. Localized emission of a red-shifted G′ band was observed by near-field Raman and photoluminescence experiments and related to the local distortion of the nanotube lattice by a negatively charged defect (65). **Figure 11** shows near-field Raman and near-field photoluminescence spectra and spatial maps for an individual SWNT. **Figure 11a** and **Figure 11b** show the photoluminescence and Raman spectra, respectively (65). **Figures 11c–f** show near-field measurements from the same SWNT. **Figure 11c** represents the near-field photoluminescence image of an SWNT where the image contrast is provided by spectral integration over the photoluminescence peak centered at $\lambda_{em} \sim 900$ nm. The most striking feature in this image is the high degree of spatial localization of the photoluminescence emission along the SWNT. This is evident by inspection of the extended topography
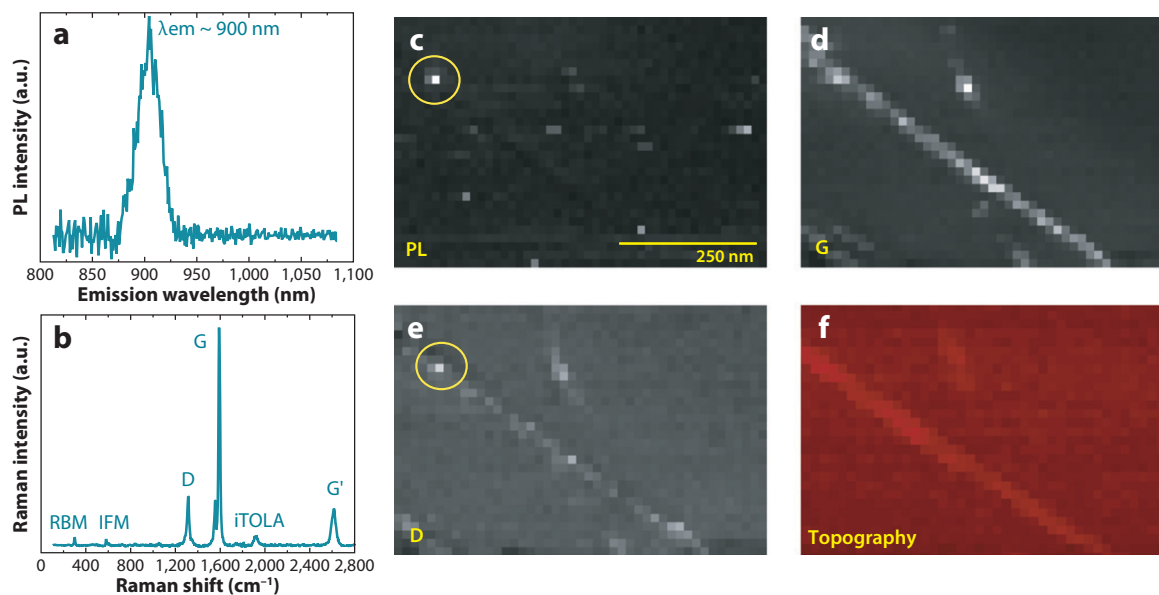

Figure 11

Localized excitonic emission in a semiconducting SWNT. (*a*) Photoluminescence (PL) emission at $\lambda_{em} \sim 900$ nm (*b*) Raman spectrum recorded from the same SWNT. The spectral position of the RBM, $\omega_{RBM} = 302$ cm^{-1}, with the $\lambda_{em} = 900$ nm information, leads to the (9,1) assignment. (*c*) Near-field photoluminescence image of the SWNT revealing localized excitonic emission. (*d–e*) Near-field Raman imaging of the same SWNT, where the image contrast is provided by spectral integration over the G and D bands, respectively. (*f*) Corresponding topography image. The yellow circles indicate localized photoluminescence (*c*) and defect-induced (D-band) Raman scattering (*e*). The scale bar in part *c* denotes 250 nm (65).

image of the nanotube shown in **Figure 11f** and of the near-field Raman image of the G band with a peak intensity near 1590 cm^{-1} shown in **Figure 11d**. Whereas we observe that the G-band Raman scattering is present along the entire length of the 900-nm nanotube in **Figure 11d**, we observe an increased defect-induced (D-band, 1300 cm^{-1}) Raman scattering intensity localized in the same region where exciton emission was detected in **Figure 11e**.

Interestingly, when measuring the Raman spectra across the defective spot using near-field spectroscopy, sudden changes in many Raman features are observed. Maciel et al. (65) have shown that substitutional doping in SWNTs causes changes in the G′-band spectra due to charge-induced renormalization of the electronic and vibrational energies. Consequently, *n*- and *p*-type doping can be differentiated by a negative and positive shift of the G′ frequency measured near the defect site. It is clear that near-field Raman spectroscopy opens up a new world for exploration. Although this research area still presents several technical difficulties, near-field techniques seem to provide major future opportunities for Raman spectroscopy studies on nanocarbons.

4. CONCLUDING REMARKS

We review the basic aspects of resonance Raman spectroscopy used to study graphitic (sp^2-bonded carbons) systems, such as single- and few-layers graphene, graphite, and carbon nanotubes. All made by a single atom species, namely carbon, such systems provide a unique material for studying very detailed modifications and interactions at the nanoscale level. The weak interaction between graphene layers, the effect of folding a single layer into a nanotube, and the presence of defects at the atomic level and as an extended structure (such as at a graphene interface) can be studied in detail using the double-resonance Raman process. The strong coupling between phonons and electrons near the Fermi level generate measurable modifications to the electronic and vibrational structure, and these modifications adjust with changes in the Fermi level, thus providing information about natural or intentional doping. The diameter-dependent RBMs of carbon nanotubes give detailed information about the one-dimensional confinement of their electronic structure, thus giving information about the unusually strong Coulomb coupling between optically generated electrons and holes (i.e., about excitons). This combined knowledge allows a detailed study of environmental perturbations in these materials, generally described by the effect of van der Waals and dielectric screening-based interactions. The possibility of studying near-field Raman spectroscopy drives these efforts into a new realm, where these very detailed modifications and interactions occurring at the nanoscale level can be probed locally.

DISCLOSURE STATEMENT

The authors are not aware of any affiliations, memberships, funding, or financial holdings that might be perceived as affecting the objectivity of this review.

ACKNOWLEDGMENTS

LITERATURE CITED

1. Dresselhaus MS, Dresselhaus G, Saito R, Jorio A. 2005. *Phys. Rep*. 409:47–99
2. Jorio A, Pimenta MA, Souza Filho AG, Saito R, Dresselhaus G, Dresselhaus MS. 2003. *N. J. Phys*. 5:139.1–17
3. Saito R, Grüneis A, Samsonidze GG, Brar VW, Dresselhaus G, et al. 2003. *N. J. Phys*. 5:157.1–15
4. Pimenta MA, Dresselhaus G, Dresselhaus MS, Cançado LG, Jorio A, Saito R. 2007. *Phys. Chem. Chem. Phys*. 9:1276–91
5. Saito R, Dresselhaus G, Dresselhaus MS. 1998. *Physical Properties of Carbon Nanotubes*. London: Imperial Coll. Press
6. Malard LM, Guimares MHD, Mafra DL, Massoni MSC, Jorio A. 2009. *Phys. Rev. B*. 79:125426
7. Jorio A, Saito R, Dresselhaus MS. 2010. *Raman Spectroscopy in Nanoscience and Nanometrology: Carbon Nanotubes, Nanographite and Graphene*. WeinHeim, Ger.: Wiley-VCH Verlag GmbH & Co KGaA. In press
8. Farhat H, Son H, Samsonidze GG, Reich S, Dresselhaus MS, Kong J. 2007. *Phys. Rev. Lett*. 99:145506
9. Sasaki K, Saito R, Dresselhaus G, Dresselhaus MS, Farhat H, Kong J. 2008. *Phys. Rev. B* 77:245441
10. Tuinstra F, Koenig JL. 1970. *J. Phys. Chem*. 53:1126–30
11. Sato K, Saito R, Oyama Y, Jiang J, Cançado LG, et al. 2006. *Chem. Phys. Lett*. 427:117–21
12. Rao AM, Richter E, Bandow S, Chase B, Eklund PC, et al. 1997. *Science* 275:187–91
13. Jorio A, Saito R, Hafner JH, Lieber CM, Hunter M, et al. 2001. *Phys. Rev. Lett*. 86:1118–21
14. Lazzeri M, Attaccalite C, Wirtz L, Mauri F. 2008. *Phys. Rev. B* 78:R081406–9
15. Dresselhaus MS, Dresselhaus G, Sugihara K, Spain IL, Goldberg HA. 1988. *Graphite Fibers and Filaments. Springer Ser. Mater. Sci.*, 5:1–382. Berlin: Springer-Verlag
16. Malard LM, Pimenta MA, Dresselhaus G, Dresselhaus MS. 2009. *Phys. Rep*. 473:51–87
17. McClure JW. 1957. *Phys. Rev*. 108:612–18
18. Slonczewski JC, Weiss PR. 1958. *Phys. Rev*. 109:272–79
19. Novoselov KS, Geim AK, Morozov SV, Jiang D, Zhang Y, et al. 2004. *Science* 306:666–69
20. Geim AK. 2009. *Science* 324(5934):1530–34
21. Novoselov KS, Geim AK, Morozov SV, Jiang D, Katsnelson MI, et al. 2005. *Nature* 438:197–200
22. Geim AK, Novoselov KS. 2007. *Nat. Mater*. 6:183–91
23. Affoune A, Prasad BLV, Sato H, Enoki T, Hishiyama Y, Kaburagi Y. 2001. *Chem. Phys. Lett*. 348:17–20
24. Berger C, Song Z, Li T, Li X, Ogbazghi AY, et al. 2004. *J. Phys. Chem. B* 108:19912–16
25. Berger C, Song Z, Li X, Wu X, Brown N, et al. 2006. *Science* 312:1191–96
26. Reina A, Thiele S, Jia X, Bhaviripudi S, Dresselhaus MS, et al. 2009. *Nano Res*. 2:509–16
27. Dresselhaus MS, Dresselhaus G, Eklund PC. 1996. *Science of Fullerenes and Carbon Nanotubes*. New York/San Diego, CA: Academic
28. Dresselhaus MS, Dresselhaus G. 1982. *Light Scattering in Graphite Intercalation Compounds, Light Scattering in Solids III*. Vol. 51: *Top. Appl. Phys.*, ed. M Cardona, G Güntherodt, pp. 3–57. Berlin: Springer-Verlag.
29. Reich S, Jantoljak H, Thomsen C. 2000. *Phys. Rev. B* 61:R13389–92
30. Grüneis A. 2004. *Resonance Raman spectroscopy of single wall carbon nanotubes*. PhD thesis. Tohoku Univ. 120 pp.
31. Reich S, Thomsen C. 2004. *Philos. Trans. Ser. A* 362:2271–88

32. Saito R, Jorio A, Souza Filho AG, Dresselhaus G, Dresselhaus MS, Pimenta MA. 2001. *Phys. Rev. Lett.* 88:027401

33. Park JS, Reina A, Saito R, Kong J, Dresselhaus G, Dresselhaus MS. 2009. *Carbon* 47:1303–10

34. Malard LM, Elias DC, Alves ES, Pimenta MA. 2008. *Phys. Rev. Lett.* 101:257401

35. Ando T. 2007. *J. Phys. Soc. Jpn.* 76:104711

36. Jorio A, Souza Filho AG, Dresselhaus G, Dresselhaus MS, Swan AK, et al. 2002. *Phys. Rev. B* 65:155412

37. Brown SDM, Jorio A, Corio P, Dresselhaus MS, Dresselhaus G, et al. 2001. *Phys. Rev. B* 63:155414

38. Park JS, Sasaki K, Saito R, Izumida W, Kalbac M, et al. 2009. *Phys. Rev. B* 80:R081402

39. Kalbac M, Farhat H, Kavan L, Kong J, Sasaki K, et al. 2009. *ACS Nano* 3:2320–28

40. Farhat H, Sasaki K, Kalbac M, Hofmann M, Saito R, et al. 2009. *Phys. Rev. Lett.* 102:126804

41. Saito R, Dresselhaus G, Dresselhaus MS. 2000. *Phys. Rev. B* 61:2981–90

42. Kataura H, Kumazawa Y, Kojima N, Maniwa Y, Umezu I, et al. 1999. In *Proc. Int. Winter Sch. Electron. Prop. Novel Mater. (IWEPNM'99)*, ed. H Kuzmany, M Mehring, J Fink, *AIP Conf. Proc.* 486, pp. 328–32

43. Bachilo SM, Strano MS, Kittrell C, Hauge RH, Smalley RE, Weisman RB. 2002. *Science* 298:2361–66

44. Araujo PT, Jorio A. 2008. *Phys. Status Solidi B* 245:2201–4

45. Hata K, Futaba DN, Mizuno K, Namai T, Yumura M, Iijima S. 2004. *Science* 306:1362–65

46. Joselevich E, Dai H, Liu J, Hata K, Windle A. 2008. *Top. Appl. Phys.* 111:101–64

47. Araujo PT, Doorn SK, Kilina S, Tretiak S, Einarsson E, et al. 2007. *Phys. Rev. Lett.* 98:067401

48. Doorn SK, Araujo PT, Hata K, Jorio A. 2008. *Phys. Rev. B* 78:165408

49. Samsonidze GG, Saito R, Jorio A, Pimenta MA, Souza Filho AG, et al. 2003. *J. Nanosci. Nanotechnol.* 3:431–58

50. Saito R, Sato K, Oyama Y, Jiang J, Samsonidze GG, et al. 2005. *Phys. Rev. B* 72:153413

51. Araujo PT, Pesce PBC, Dresselhaus MS, Sato K, Saito R, Jorio A. 2010. *Physica* 42(5):1251–61

52. Kane CL, Mele EJ. 2003. *Phys. Rev. Lett.* 93:197402

53. Araujo PT, Jorio A, Dresselhaus MS, Sato K, Saito R. 2009. *Phys. Rev. Lett.* 103:146802

54. Samsonidze GG, Saito R, Kobayashi N, Grüneis A, Jiang J, et al. 2004. *Appl. Phys. Lett.* 85:5703–5

55. Jiang J, Saito R, Sato K, Park JS, Samsonidze GG, et al. 2007. *Phys. Rev. B* 75:035405

56. Jiang J, Saito R, Samsonidze GG, Jorio A, Chou SG, et al. 2007. *Phys. Rev. B* 75:035407

57. Araujo PT, Maciel IO, Pesce PBC, Pimenta MA, Doorn SK, et al. 2008. *Phys. Rev. B* 77:R241403

58. Ohno Y, Iwasaki S, Murakami Y, Kishimoto S, Maruyama S, Mizutan T. 2006. *Phys. Rev. B* 73:235427

59. Miyauchi Y, Saito R, Sato K, Ohno Y, Iwasaki S, et al. 2007. *Chem. Phys. Lett.* 442:394–99

60. Saito R, Sato K, Araujo PT, Jorio A, Dresselhaus G, Dresselhaus MS. 2009. *Phys. Status Solidi B* 246:2581–85

61. Ando T. 1997. *J. Phys. Soc. Jpn.* 66:1066–73

62. Perebeinos V, Tersoff J, Avouris P. 2004. *Phys. Rev. Lett.* 92:257402

63. Paillet M, Poncharal P, Zahab A. 2006. *Phys. Rev. Lett.* 96:039704

64. Samsonidze GG, Saito R, Jorio A, Souza Filho AG, Grüneis A, et al. 2003. *Phys. Rev. Lett.* 90:027403

65. Maciel IO, Anderson N. Pimenta MA, Hartschuh A, Qian H, et al. 2008. *Nat. Mater.* 7:878–83

66. Ando T. 2010. *J. Phys. Soc. Jpn.* 79:024707

67. Sasaki K, Farhat H, Saito R, Dresselhaus MS. 2010. *Physica E.* 42:2005

**Annual Review of
Condensed Matter
Physics**

Volume 1, 2010

Contents

Errata

An online log of corrections to *Annual Review of Condensed Matter Physics*
articles may be found at http://conmatphys.annualreviews.org/errata.shtml